Growth of Cu_2ZnSnS_4 absorber layer on flexible metallic substrates for thin film solar cell applications

Sebnem Yazici [a], Mehmet Ali Olgar [b], Fatime Gulsah Akca [a], Ayten Cantas [a], Metin Kurt [a], Gulnur Aygun [a], Enver Tarhan [a], Ekrem Yanmaz [b], Lutfi Ozyuzer [a,*]

[a] Department of Physics, Izmir Institute of Technology, Urla, Izmir 35430, Turkey
[b] Department of Physics, Karadeniz Technical University, Trabzon, Turkey

ARTICLE INFO

ABSTRACT

In this work, Cu_2ZnSnS_4 (CZTS) absorber layers were fabricated using a two-stage process. Sequentially deposited Cu–Zn–Sn thin film layers on metallic foils were annealed in an $Ar + S_{2(g)}$ atmosphere. We aimed to investigate the role of flexible titanium and molybdenum foil substrates in the growth mechanism of CZTS thin films. The Raman spectra and X-ray photoelectron spectroscopy analyses of the sulfurized thin films revealed that, except for the presence of Sn-based secondary phases, nearly pure CZTS thin films were obtained. Additionally, the intense and sharp X-ray diffraction peak from the (112) plane provided evidence of good crystallinity. Electron dispersive spectroscopy analysis indicated sufficient sulfur content but poor Zn atomic weight percentage in the films. Absorption and band-gap energy analyses were carried out to confirm the suitability of CZTS thin films as the absorber layer in solar cell applications. Hall effect measurements showed the p-type semiconductor behavior of the CZTS samples. Moreover, the back contact behavior of these metallic flexible substrates was investigated and compared. We detected formation of cracks in the CZTS layer on the molybdenum foils, which indicates the incompatibility of molybdenum's thermal expansion coefficient with the CZTS structure. We demonstrated the application of the magnetron sputtering technique for the fabrication of CZTS thin films on titanium foils having lightweight, flexible properties and suitable for roll-to-roll manufacturing for high throughput fabrication. Titanium foils are also cost competitive compared to molybdenum foils.

© 2015 Elsevier B.V. All rights reserved.

1. Introduction

To meet the worldwide energy demand in green technology in a cost competitive way, cheap and readily available clean energy systems are needed. Solar power is the most economic and powerful energy source among the renewable energy sources. Over the last few decades, the low cost and easy fabrication of thin film solar cell technology has allowed it to compete with conventional Si wafer technology and to take a major market share in the photovoltaic (PV) industry. Recently, the use of Cu_2ZnSnS_4 (CZTS) as an absorber layer in thin film solar cell technology has been investigated. Moreover, this material is already being considered as a replacement for conventional chalcogenide-based absorber layers ($CuIn_xGa_{1-x}Se_2$ and CdTe). In fact, this replacement is urgently needed in the PV industry due to the restrictions on the usage of the heavy metal Cd and the scarcity and high cost of In and Ga. CZTS is a p-type quaternary compound semiconductor that is stable in the kesterite structure. The CZTS kesterite crystal structure with a large absorption coefficient ($\geq 10^4$ cm^{-1}) has a band gap energy of approximately 1.4–1.6 eV [1]. Beyond these beneficial physical properties,

CZTS consists of earth-abundant, cheap, and non-toxic elements. These features have led researchers to focus on the CZTS compound for use in solar cell technology. Currently, efficiencies up to 9.2% and 12.6% have been achieved for the kesterite structures Cu_2ZnSnS_4 [2] and $Cu_2ZnSn(S,Se)_4$ [3], respectively. Theoretical calculations based on the Shockley–Queisser limit for a single p–n junction with a band gap of 1.4 eV claim that an approximately 33.7% maximum solar conversion efficiency using an AM 1.5 solar spectrum can be generated [4]. For these reasons, the CZTS compound semiconductor will be the preferred material for thin-film PVs in the immediate future.

Several methods have been used in the fabrication of CZTS thin film absorber layers, such as atomic beam sputtering [5], e-beam evaporation [6], thermal evaporation [7], magnetron sputtering [8–11], electrodeposition [12,13], spray pyrolysis deposition [14,15], pulsed laser deposition [16], etc. Most of these techniques were carried out using rigid substrates such as bilayer molybdenum (Mo) coated soda lime glass (SLG). However, the deposition of the CZTS absorber layer on flexible substrates may open a wide range of application areas for large area thin film solar cell fabrication [17]. Metallic foils, such as Cr-steels, titanium (Ti), Mo, aluminum and some alloys are promising flexible substrates because they are cheap, lightweight, durable, and resistant to high-temperature fabrication processes. Additionally, metallic flexible substrate utilization eliminates

the need for the deposition of a metallic conductive back contact layer. As a result, the cost of manufacturing and constructing solar cell modules would be substantially lowered by using flexible metallic substrates. The preferential flexible substrates should have well-matched coefficients of thermal expansion (CTE) (i.e., $5–12 \times 10^{-6}\ K^{-1}$), sufficient thermal (T ≥ 400 °C) and chemical resistivity (especially against S and Se), and should be suitable for a roll-to-roll deposition, in addition to being cost efficient [18].

Growth of CZTS layer on flexible Mo foil has only been investigated via the solvothermal approach [19]. Deposition of CZTS layers on flexible polyimide substrates was carried out using a screen printing process [20] and the electrochemical deposition technique [21]. Investigations of CZTS absorber layer growth on metallic flexible substrates via magnetron sputtering followed by sulfurization have not been reported in the literature yet.

In the present work, the magnetron sputtering technique was used in the first stage of the growth mechanism, since sputtering offers a wide range of advantages, such as easy adaptation to large-scale and reproducible manufacturing. Additionally, we chose to investigate both Ti and Mo foil substrates, due to the Ti's preferable CTE and chemical inertness behavior, as well as to compare the results of the two foils.

A chemically inert back contact layer with optimum electrical characteristics is necessary to achieve a high efficient solar cell. In the case of Mo back contact, high temperature sulfurization process leads to the decomposition of the CZTS absorber layer, resulting in MoS_2 phase formation [22,23], which restricts the hole transport from CZTS to Mo layer [24]. The interfacial MoS_2 layer may affect open circuit voltage (V_{oc}) and change the band alignment between the CZTS absorber layer and Mo substrate. Furthermore, impurities released from the substrate are another problem in the case of metal foil utilization. Pure metallic foil substrates like chromium and Ti can be used without a diffusion barrier since their diffusion rates into the absorber are comparably low [25] and have no detrimental effects on the conversion efficiency of the solar cells. Other intrinsic physical properties of the substrate, such as the CTE and surface roughness, affect the characteristics of the adjacent active layer. The CTE of the substrate and the adjacent active semiconductor layer should be in the same range. Adhesion problems may occur due to a high CTE of the substrate, while a low CTE may cause defects like crack formation. Formation of cracks decreases the performance of the device since it creates shunt paths between the back and front contacts of the device. Micro-cracks are also inactive cell domains and, thus, they reduce the active cell area. Therefore, back contact with a CTE nearly equal to that of the absorber layer is preferable to reduce the possibility of crack formation. Additionally, since surface roughness of the metal substrate causes leakage current and pinholes, surface smoothness of a metallic substrate is another important factor to achieve high efficient flexible solar cells [26]. Therefore, a smooth surface may ensure easier and more homogenous active layer deposition.

Furthermore, the choice of substrate is crucially important to reduce the manufacturing costs for the high throughput fabrication of thin film solar cells. The cost of commercially available metal foils depends on the purity level and the Earth's reserve of the element. Ti is the fourth most abundant structural metal in the Earth's crust, and it is 600 times more abundant than Mo in [27]. Consequently, Mo foil is more expensive than Ti foil. Taking these factors into consideration, the careful selection of the substrate is crucially important to equip the growing thin film industry for mass production. The objective of this study is to establish a clear understanding of the substrate and back contact behavior of these promising Ti and Mo flexible substrates.

2. Material and methods

In the present work, we used 100 μm thick and ≥99.5% pure Ti and Mo foils supplied by Sigma-Aldrich, and SLG substrate was used for optical and electrical characterization of CZTS material. Before the sputtering process, to remove the oxidized layer and decrease the surface roughness, Ti and Mo foils were chemically etched with diluted HF and HCl, respectively. Additionally, the SLG substrate was cleaned by subsequent ultrasonication in acetone, ethanol and distilled water and then dried under a nitrogen stream. The CZTS layers were grown on these three substrates via sulfurization of the stacked metallic precursors, which were deposited sequentially by a multi-target DC magnetron sputtering system using 2-inch targets of Cu (99.999%), Zn (99.99%), and Sn (99.999%) at room temperature (Fig. 1). The deposition times were adjusted to 5 min for Cu, Sn and Zn targets by tuning the sputtering power. Deposition was conducted in attempt to achieve the desired layer thicknesses in the same time span for all three targets. With this approach, we would be able to use the co-sputtering method in our future work. After a base pressure below 1.3×10^{-4} Pa was reached, the sputtering process was started. Operating pressure was maintained at 2.0 Pa, and target-to-substrate distance was fixed at 8 cm. In this way, we sequentially grew layered metallic precursors, i.e. Cu/Sn/Zn layers, on the Ti and Mo foils as well as on the SLG substrate (Fig. 1(a)). The metallic precursors were produced using the same procedure for each process. Metallic precursors on Ti and Mo foils were obtained from a single sputtering run with a double-faced sample holder apparatus (Fig. 1(c)). The sulfurization procedure was performed in a Lindberg/Blue M tube furnace. The sulfur powder (99.98%) was placed in a custom-made quartz glass tube containing a small cylindrical outer partition. The cylindrical partition was heated to approximately 130 °C via Joule heating to produce sulfur vapor. This system enabled the precursors to be quickly heated by transferring the precursor from the room temperature zone to the furnace central zone using a transfer rod (Fig. 2). The metallic precursors were loaded in the quartz tube installed in the tube furnace. Using a MKS 647C mass flow controller, 50 sccm of the carrier gas, Ar, was directed into the quartz tube during the sulfurization process. Ar was selected as the carrier gas rather than N_2 because the formation of TiN in the interface layer could deteriorate the CZTS on the foil substrate. The pressure was maintained at atmospheric pressure. The furnace temperature was set at 270 °C, and we placed the metallic precursor into the furnace using the transfer rod. The furnace temperature was raised to 560 °C in 10 °C increments per minute. Fig. 3 represents the sulfurization process parameters of the CZTS films of this study.

Then, these samples were sulfurized in this setup for two hours at 560 °C. After sulfur treatment, the current source was turned off, and just the Ar gas inlet was left on. Afterwards, the films were cooled
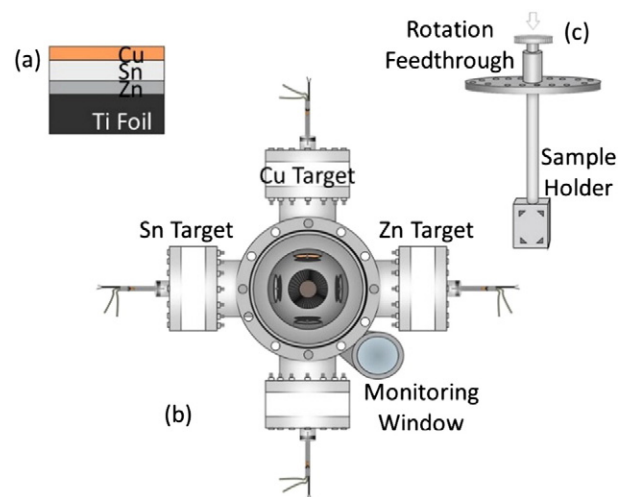

Fig. 1. (a) Illustration of sputtered metallic thin film layers on Ti foil, (b) schematic diagram of top view of multi-targeted sputtering system and (c) illustration of sample holder apparatus within the sputtering system.
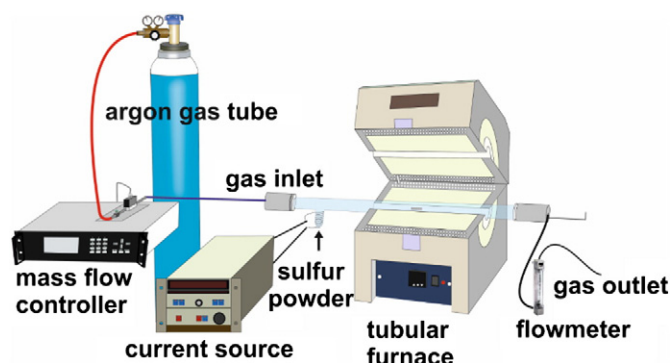
Fig. 2. Illustration of annealing setup.

naturally. We refer to these sulfurized films as Ti-CZTS on Ti foil, Mo-CZTS on Mo foil and SLG-CZTS on SLG substrates.

The crystal structures of the CZTS thin films were analyzed by X-ray diffractometry (XRD; Philipps X'Pert Pro). The XRD was operated in the Bragg–Brentano focusing geometry from 20° to 80° on a Phillips X'Pert Pro X-Ray diffractometry with Cu K_α radiation ($\lambda = 1.5406$ Å) using a step size of 0.03° and a time step of 1.1 s. Since the simultaneously formed ZnS (JCPDS: 00-05-0566) and Cu_2SnS_3 (JCPDS: 00-027-0198) secondary phases have very similar crystal structures with kesterite CZTS, XRD analysis alone is not a sufficient analysis technique to detect kesterite CZTS structure (JCPDS: 026-0575) [28]. Therefore, Raman scattering analysis was also needed to obtain a complete and reliable analysis. The high-resolution micro-Raman spectroscopy with a 100× objective (Princeton Instruments, Acton SP2750 0.750 mm Imaging Triple Grating Monochromator) was used at room temperature with the excitation wavelength of 514.5 nm. The growth morphology was investigated using a scanning electron microscope (SEM; FEI-QuantaFEG 250) by using 20 kV acceleration voltage, equipped with Energy Dispersive Spectroscopy (EDS; Oxford X-act). The EDS analysis was carried out using an LV detector (BSED), HV resolution (20 kV) and 5 spot size in high vacuum. EDS analysis of the samples gave us essential information about the stoichiometry of the films. Additionally, X-ray photoelectron spectroscopy (XPS; SPECS Phoibos 150 3D-DLD) analysis was performed to determine the chemical bonding and secondary phase formation. XPS measurements were performed with a monochromatized Mg K_α radiation source ($h\nu = 1254$ eV) with a power of 200 W. The analyzer pass energy and the step size were set to 30 eV and 0.1 eV, respectively. The spectra were referenced with respect to C 1 s peak at 284 eV [29]. After applying the Shirley background subtraction, the deconvolution process of the spectra was done with Gaussian–Lorentzian peak profile using CasaXPS software.
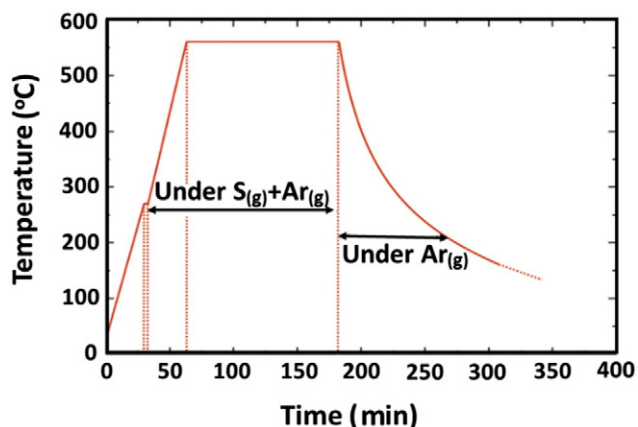

Fig. 3. Sulfurization temperature and heating rate profile.

The SLG-CZTS samples were investigated to determine electrical and optical characteristics. Four point probe measurements (Keithley 2182A nanovoltmeter, Keithley 7001 switch system, Keithley 220 programmable current source) and Hall effect measurements (Lakeshore 450 Gaussmeter and Phywe 06480.01 electromagnet) were performed to measure the sheet resistance, resistivity, carrier concentration, and mobility of the CZTS semiconducting compounds. A PerkinElmer Lambda 950 UV/VIS/NIR spectrometer was used for optical measurements. Optical absorption and transmission measurements were conducted for band-gap calculations. The film thicknesses were measured by a Veeco DEKTAK 150 surface profilometer.

3. Results and discussion

3.1. Etching process

As-purchased metal foils have rough surface arising from the foil production process. In order to get rid of the textured surface of foils, polishing or coating a leveling layer is necessary for foil substrate utilization [18]. For this reason, the Ti and Mo foils were chemically etched with diluted HF and HCl, respectively, before the sputtering process. The Ti and Mo foils' surface roughness values were examined by AFM spectroscopy before and after etching. A decrement was observed in the surface roughness of the Ti foil. However, the Mo foil surface became rougher after the etching process (Table 1). Due to the highly scratched surface of as-purchased Mo foil, scratch lines became deeper after etching with HCl.

Additionally, a passive oxide film on the Ti surface spontaneously forms when exposed to air at room temperature. This passive film forms an amorphous structure and is composed of three layers; firstly, TiO forms adjacent to the metallic Ti, followed by a Ti_2O_3 layer, and followed by TiO_2, which is in contact with the environment [30]. This amorphous oxide film crystallizes into anatase at about 276 °C, remains in an anatase structure in the range of 276–457 °C, and contains both anatase and rutile sublayers in the range of 457–718 °C [31]. This intervening oxide layer is detrimental in creating an ohmic contact between the CZTS and Ti metal substrate. We aimed to etch this amorphous passive oxide layer before sputtering, since the subsequent process, sulfurization, requires a heat treatment higher than 500 °C.

A mixed acid solution treatment is a common method employed to remove the oxide layer and contaminations from surfaces. According to the literature, there are five acid solutions in use to remove the oxide layer from Ti surfaces. A standard acid solution is composed of either HF or a combination of HF and HNO_3 in distilled water [32]. Takeuchi et al. studied three other solutions, $Na_2S_2O_8$, H_2SO_4, and HCl, to determine their decontamination effects on Ti surfaces [33]. We chose an HF solution in distilled water to remove the oxide layer from the Ti foil. Our study confirmed that the oxide layer was successfully removed using HF in distilled water.

To ensure the removal of the native oxide layers, CZTS layers grown on untreated and etched Mo and Ti foils were analyzed and compared with each other. The removal of the Ti-oxide layer can be clearly seen in the XRD (Fig. 4(a)) and Raman analysis (Fig. 4(b)). The diffraction peaks resulting from the rutile and anatase TiO_2 are more intensive for untreated Ti-CZTS than those of etched samples. Similarly, Raman analysis of untreated Ti-CZTS revealed the existence of the rutile phases with the peaks located at 445 and 610 cm^{-1} [34]. The characteristic

Table 1
Surface roughness of Mo and Ti foils before and after etching (scan size: 5 μm) (R_a: arithmetic average).

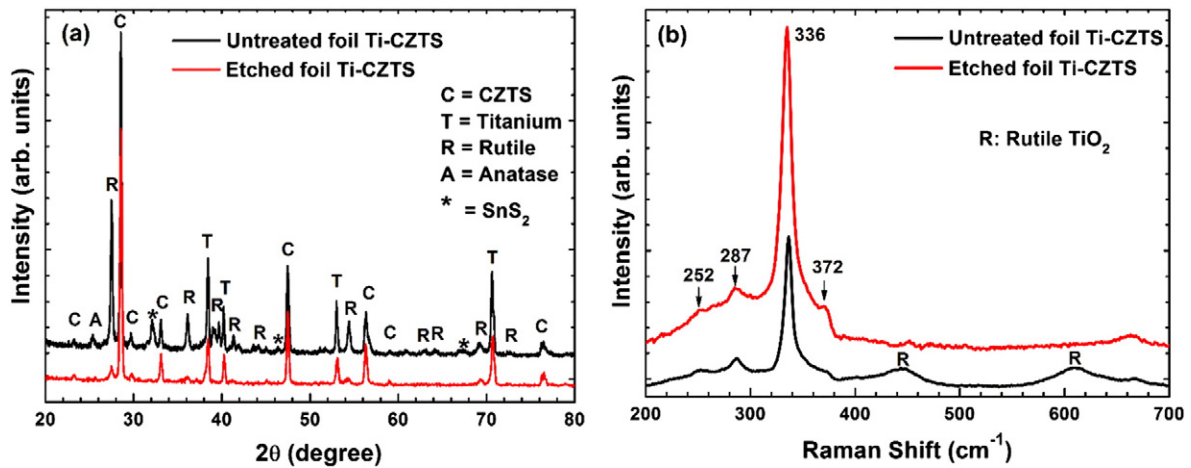| Surface roughness (R_a, nm)		
	Before etching	After etching
Mo Foil	24.905	26.131
Ti Foil	33.342	22.199

Fig. 4. Untreated (black) and etched (red) foil Ti-CZTS (a) XRD diffractograms and (b) Raman spectroscopy.

vibration modes of CZTS material are located at 337, 288, 252 and 372 cm^{-1} [35].

Since TiO$_2$ is a native oxide that grows at elevated temperatures, it has physical properties (e.g. CTE, lattice size) similar to the native material. This means that the thin oxide layer on Ti foil would not create significant stresses in the material. However, removal of the oxide layer is important to create a low-resistance and stable ohmic contact between the back contact material and p-type semiconductor.

In the same way, we compared the XRD plots of CZTS material deposited on untreated and etched Mo foil substrates (Fig. 5(a)). Except the small peaks indicating SnO$_2$ formation, there are not any prominent oxide peaks related to Mo. The relative intensity of the preferential plane (112) of the CZTS structure is considerably higher than that of non-etched Mo-CZTS sample. In Fig. 5(b), there are no any traces of the oxidized layer in the Raman spectroscopy for the untreated Mo foil. Additionally, the characteristic Raman peak at 336 cm^{-1} is more intensive for etched than that of untreated Mo-CZTS. Even though surface roughness was increased after etching, Raman and XRD analysis revealed good outcomes. Therefore, we preferred to use etched Mo foils.

3.2. Compositional and morphological analyses

The thicknesses of the Cu/Sn/Zn layers were measured 155, 360, and 175 nm, respectively, using the profilometer. These thicknesses were calculated through molecular weight and density calculations of each elements. Because CZTS is a quaternary semiconducting compound, it exhibits a very complex structure. Therefore, its formation requires systematic control of sputtering conditions in both stages during the growth of the CZTS layer. In the first stage of the process (depositing the metallic precursor), the sputtering method allows for easy adjustment of the metallic content by changing the sputtering time and power. Metallic sputtering targets were used to deposit CZTS absorber layers in a cost-effective way. Temperature and duration play major roles during the sulfurization process of the metallic precursors to form the CZTS compound. The compositional analysis was done with EDS measurements, and the growth morphology of the layers was analyzed with SEM imaging. Fig. 6 represents the SEM images of Mo-CZTS, Ti-CZTS and SLG-CZTS samples.

Producing a microstructure with larger grains is possible using metallic targets, but surface homogeneity can be a problem, including voids and agglomerations of Sn in some regions. It was asserted that sulfur introduction into the metallic precursors with sulfur containing targets ensures uniform and denser layers [36]. Incorporation of sulfur into the metallic precursor during the sulfurization process results in an expansion of the film with rising sulfur content, which can cause stress and voids in the CZTS layer [37]. As shown in Table 2, the atomic compositions of the samples are similar to each other in that both are poor in Zn and rich in Sn. By combining Table 2 and Fig. 6, it can be seen that
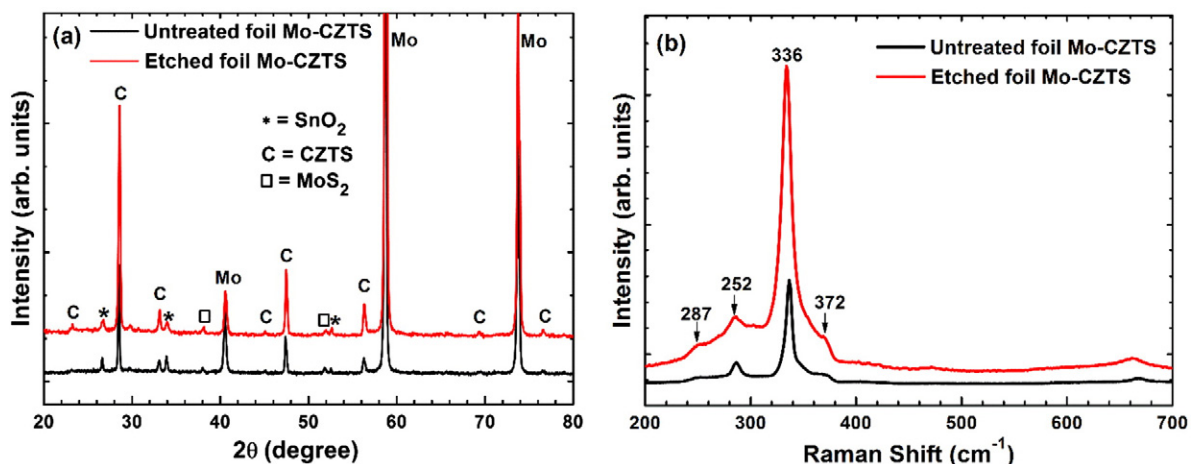

Fig. 5. Untreated (black) and etched (red) foil Mo-CZTS (a) XRD diffractograms and (b) Raman spectroscopy.
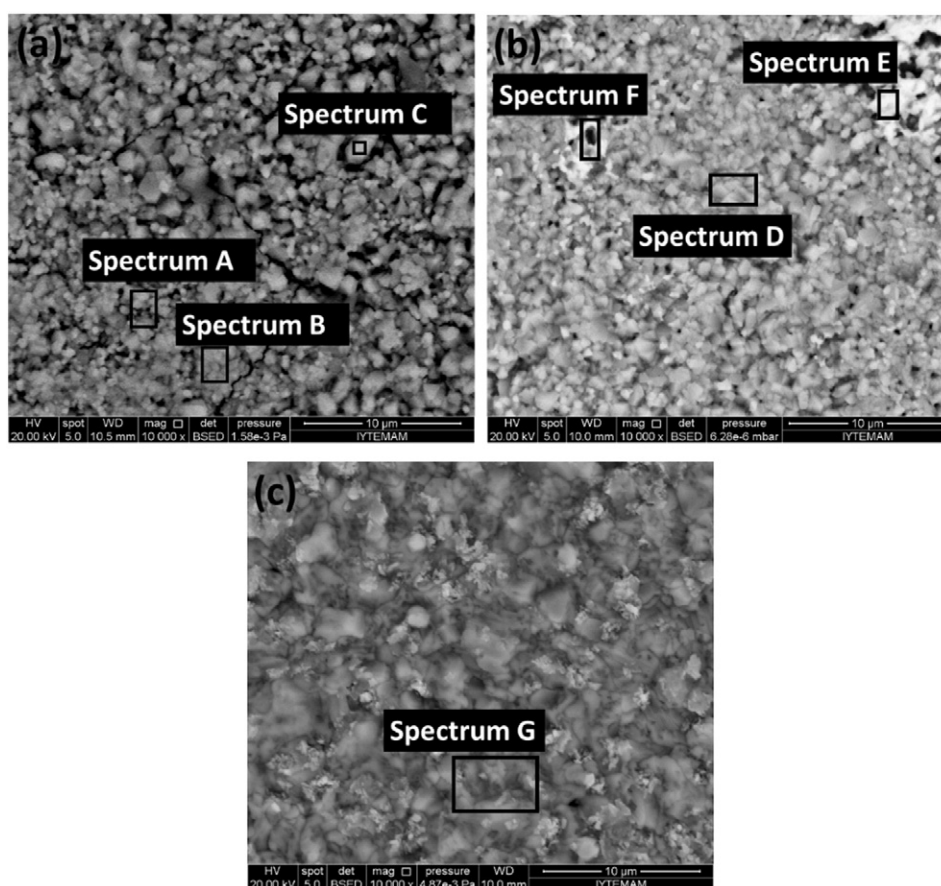
Fig. 6. Micrographs of the sulfurized films and EDS measurements of distinctive regions on (a) Mo-CZTS, (b) Ti-CZTS and (c) SLG-CZTS.

spectrum B in Mo-CZTS and spectrum D in Ti-CZTS occupy larger areas and are distributed more uniformly within the samples. The brighter colored crystal structures of spectrum E indicate an accumulation of crystals. EDS measurements revealed that this region was composed of Sn rich crystals. Spectrum F is an example of voids. In Mo-CZTS, spectrum C has a distinct crystal growth. EDS measurement revealed that these larger sized crystals indicate $Cu_{2-x}S$ formation.

Table 3 lists the chemical composition ratios of Cu/[Zn + Sn], Zn/Sn and S/[Cu + Sn + Zn] for Mo-CZTS and Ti-CZTS. It indicates that Cu-poor composition was obtained in both samples. It is given in the literature that CZTS samples with a Cu/[Zn + Sn] ratio lower than that of the stoichiometric case lead to higher conversion efficiency [38]. The fact that the Zn/Sn ratio is less than the unity indicates that each film has poorer Zn content than that of Sn. Since the composition is directly related to the sulfur content during the sulfurization, the S/[Cu + Sn + Zn] ratio should be greater than the unity in the EDS results. The ratio S/[Cu + Sn + Zn] indicates that the sulfurization stage was carried out efficiently.

Microstructures of film surfaces were investigated by SEM. The SEM images of Mo-CZTS films are shown in Fig. 7. The crack formation on the layer is noticeably evident, and one of the cracks is at the upper right in Fig. 7(b). It is well-known that the low thermal expansion of Mo (4.8×10^{-6} K^{-1}) is responsible for this deformation [39]. In contrast, crack formation or delamination was not observed in the Ti-CZTS samples (Fig. 8). Fig. 9 shows the cross-sectional image of the SLG-CZTS sample. The thickness of the CZTS layer measured in the cross-sectional image was 1.8 μm.

3.3. Structural analyses

Fig. 10 shows the results of XRD analysis of Ti-CZTS, Mo-CZTS and SLG-CZTS. The diffraction peaks from the (112), (220), (312), (224) and (332) planes with small peaks at 37.10° (202), 38.00° (211), and 44.09° (105) and (213) indicate the formation of kesterite CZTS for all three samples (JCPDS 26-0575). However, as mentioned earlier, the result of XRD analysis alone are unreliable due to the similarity of the lattice parameters of Cu_2SnS_3 and ZnS phases which probably form during the growth of the CZTS layer. Therefore, the comparison of XRD diffractograms and Raman spectra produce a more accurate analysis [40–42].

According to Fig. 10(a), the XRD pattern of the Ti-CZTS film has diffraction peaks from the Ti substrate at $2\theta = 27.45, 38.39, 40.31, 53.06$ and

Table 2
EDS results of the constituent elements of sulfurized CZTS films on Mo, Ti foils and SLG.

	Spectrum	Cu (atomic %)	Zn (atomic %)	Sn (atomic %)	S (atomic %)
Mo-CZTS	A	23.31	11.01	13.74	51.94
	B	22.78	10.71	13.49	53.02
	C	22.81	10.83	12.74	53.62
Ti-CZTS	D	22.74	11.33	13.81	52.12
	E	9.23	4.80	34.07	51.91
	F	19.72	9.64	17.56	53.08
SLG-CZTS	G	24.29	11.33	13.79	50.40

Table 3
The component ratio of the sulfurized CZTS films of Mo-CZTS and Ti-CZTS.

	Spectrum	Cu/Zn + Sn	Zn/Sn	S/Cu + Zn + Sn
Mo-CZTS	B	0.94	0.79	1.12
Ti-CZTS	D	0.90	0.82	1.08

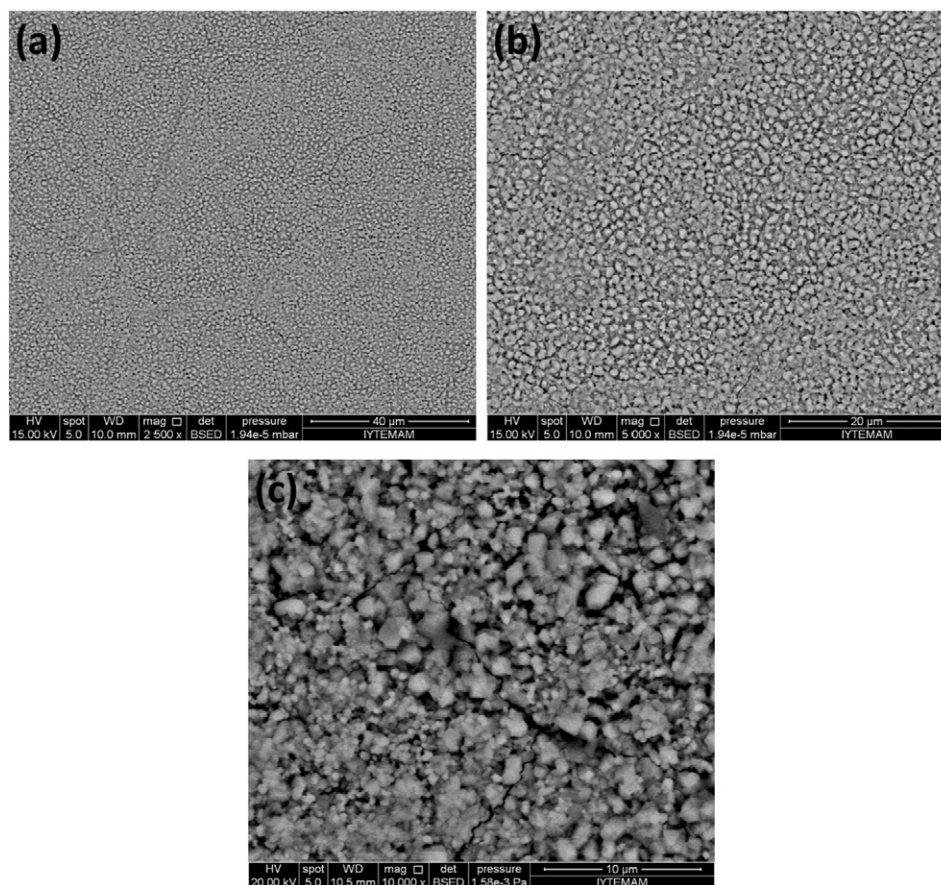**Fig. 7.** SEM images of Mo-CZTS at (a) 2.50 k×, (b) 5.00 k× and (c) 10.00 k× magnifications.

70.69° indicating the existence of the rutile phase of TiO_2 [(JCPDS no: 88-1175 and 84-1286)]. It is clear that the peaks from potential secondary phases are not present. However in the XRD pattern of Mo-CZTS displayed in Fig. 10(b), in addition to major peaks, binary secondary phases of SnS at $2\theta = 26.7°$, Cu_2S at $2\theta = 33.6°$ and SnS_2 at $2\theta = 51.97$, 52.73° were detected. After XRD analyses of our Mo foils, the diffraction peaks at $2\theta = 58.72$ and 73.68° were attributed to the Mo element itself. Lastly, in Fig. 10(c), the XRD pattern of the SLG-CZTS film exhibits nearly the same diffraction pattern as Mo-CZTS. The diffraction patterns of the films correspond to those of the EDS results with excessive content of Sn implying tin sulfide secondary phases.

Fig. 11 shows the relative intensities of main peaks with respect to the (112) preferential plane of Ti-CZTS, Mo-CZTS and reference CZTS obtained from the database. The experimental conditions for Ti-CZTS and Mo-CZTS diffractograms were kept the same. The intensities for each diffraction peaks in the experimental diffractograms were compared with the equivalent diffractograms for the powder reference, JCPDS 026-057.

Fig. 12 shows the Raman spectra of Ti-CZTS, Mo-CZTS and SLG-CZTS. In all plots, kesterite CZTS vibration modes were clearly observed. The main Raman mode was detected for Ti-CZTS, Mo-CZTS and SLG-CZTS respectively at 335, 336 and 336 cm^{-1}. The redshift in the Raman modes for Ti-CZTS and Mo-CZTS could be attributed to the tensile stress in the foils. Additionally, this shift was related to the degradation of crystalline qualities in the samples. To analyze the presence of possible secondary phases, the particular Raman modes of these phases must be known. It has been reported that there is a single Raman peak for SnS_2 at 314 cm^{-1}, while SnS has three peaks at 160, 190 and 219 cm^{-1} [43]. $Cu_{2-x}S$ has a peak at 475 cm^{-1} [44]. The strong peak in the CZTS Raman spectra at approximately 338 cm^{-1} is attributed to the vibration of S atoms having A_1 symmetry [45]. Due to the chemically inert behavior

of Ti, no vibrational modes of titanium sulfide compounds (TiS_2 or TiS_3) were observed in Raman spectrum for Ti-CZTS (Fig. 12(a)). In Fig. 12(b), the peak at 460 cm^{-1} is attributed to the presence of an impurity phase from the Mo foil substrate in Mo-CZTS. Fig. 12(c) shows Raman spectroscopy results for SLG-CZTS. The broad shoulder between 368–372 cm^{-1} and the peaks located at 336 and 287 cm^{-1} correspond to CZTS structure. Additionally, the small peak at 310 cm^{-1} indicates the SnS_2 secondary phase formation in SLG-CZTS.

3.4. Chemical analysis

The compound elements and secondary phase formations were also investigated using XPS. The surface spectrum of CZTS films shows C 1 s peak with negligible intensity, indicating that the surfaces of the films are clean enough after brief exposure to air. The presence of Cu, Zn, Sn and S elements was identified from the survey spectra of CZTS films. In addition to the survey scan, the core level spectra of Cu 2p, Zn 2p, Sn 3d and S 2p were also recorded by using narrow and detailed scan spectra to determine their valence states.

In Table 4, the deconvolution results of the core level spectra are listed. Fig. 13(a) shows the core level spectrum of Cu $2p_{3/2}$ and $2p_{1/2}$ with a peak splitting of 19.8 eV and 19.7 eV for Mo-CZTS [46] and Ti-CZTS [47], respectively. These peak splitting values are indicative of monovalent copper, Cu (I), which is consistent with the reported literature values [48–50].

The XPS measurement for Zn 2p is given in Fig. 13(b). Since Zn $2p_{3/2}$ and $2p_{1/2}$ peaks with a peak splitting of 23.1 eV for Mo-CZTS [51] and 23.0 eV for Ti-CZTS [49] are close to the standard splitting value of 22.9 eV, they confirm the bivalent character, Zn (II) [47]. For both Mo-CZTS and Ti-CZTS, the Zn $2p_{3/2}$ peak appears at 1021.3 eV which coincides with Zn in CZTS. Zn atoms in ZnS are observed at approximately
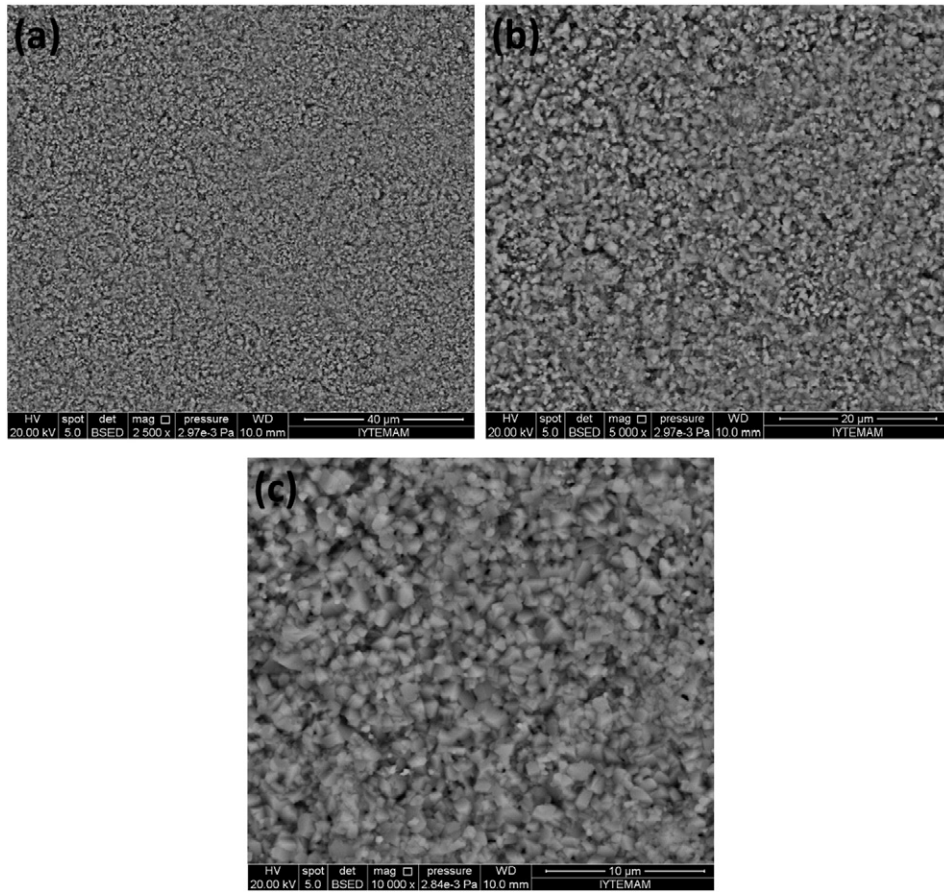
Fig. 8. SEM images of Ti-CZTS at (a) 2.50 k×, (b) 5.00 k× and (c) 10.00 k× magnifications.

1022 eV [52]. In the literature, it is possible to encounter different reported binding energy values for ZnS, most probably due to the calibration difference [49]. With reference to this, the formation of a secondary ZnS phase was not observed in either film, which is in harmony with EDS and XRD results.

Sn 3d peaks consist of a doublet with a spin-orbit splitting of 8.5 eV for Mo-CZTS [53,54] and 8.4 eV for Ti-CZTS [51,55], which is in agreement what is reported in the literature. On the other hand, Sn $3d_{5/2}$ core level peak observed at 486 eV [56] for Mo-CZTS and 485.9 eV for Ti-CZTS corresponds to the Sn in SnS phase [57]. This is consistent with the XRD patterns of CZTS thin films with a Sn-based secondary phase.

The sulfur 2p core level spectrum which is observed in the range of 160 eV to 164 eV [47,48,54] was deconvoluted as a result of spin orbit splitting in Fig. 13(d) and (e). The measurements of S 2p were taken from the 5 and 3 different regions of radius 2 mm for Mo-CZTS and Ti-CZTS, respectively. Since the S 2p signals were not clear enough when compare with other elements in CZTS, the average of these signals
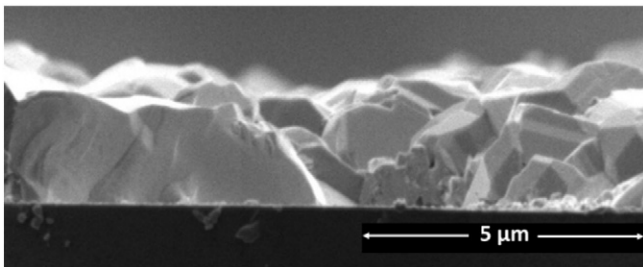

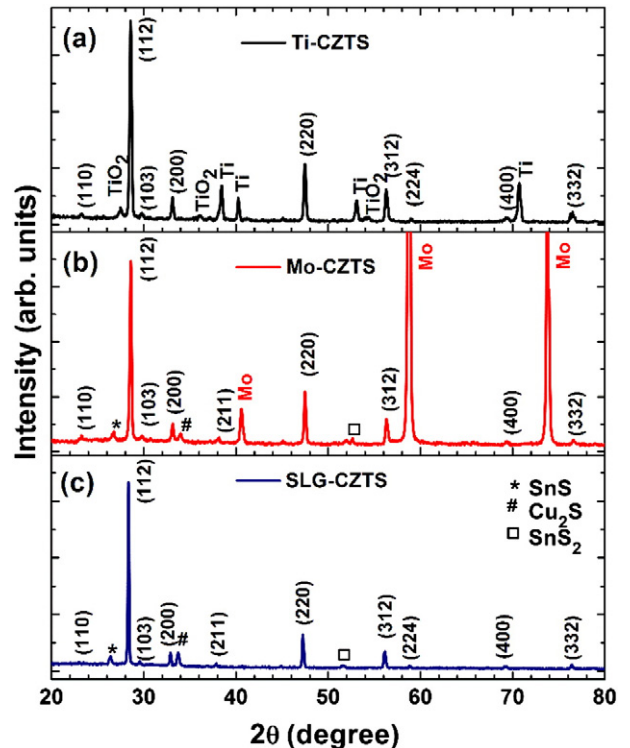**Fig. 9.** Cross-sectional image of SLG-CZTS.

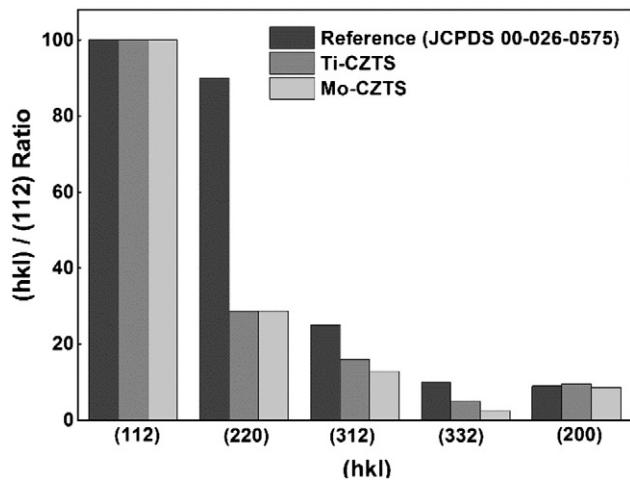**Fig. 10.** XRD diffractograms of the CZTS layer of (a) Ti-CZTS,(b) Mo-CZTS and (c) SLG-CZTS.

Fig. 11. Histogram of (hkl)/(112) preferential plane ratio of CZTS structure deposited on two different foil substrates.

were taken in the same binding energy scale and then were fitted after Shirley background subtraction using CasaXPS software by using peak fitting function of a Gaussian Lorentzian product GL(p) where "p" corresponds to Lorentzian character. The fit was obtained for the 20% Gaussian, 80% Lorentzian weighting for all synthetic peaks for Ti-CZTS and Mo-CZTS. Each doublet is constrained to have a binding energy difference of 0.7 eV between the S $2p_{3/2}$ and S $2p_{1/2}$, equal full width at half maximum (FWHM) values of 0.91 eV for all components of Ti-CZTS and Mo-CZTS, as well as a $2p_{1/2}$:$2p_{3/2}$ intensity ratio 1:2 (Table 5). The Marquardt algorithm was used during fitting process. The goodness of fit for synthetic peaks were determined with "root mean square (rms)" which is frequently used measure of the differences between predicted by a model and the observed values. The closer the fit is to the data points, the closer will be the value of rms to zero. The fitting of the synthetic peaks were obtained with "rms" values as 0.28 and

Fig. 12. Raman spectroscopy of (a) Mo-CZTS, (b) Ti-CZTS and (c) SLG-CZTS.

Table 4
The core level peak positions of sulfurized CZTS films of Mo-CZTS and Ti-CZTS.

	Binding energy values (eV)					
	Cu		Sn		Zn	
	$2p_{3/2}$	$2p_{1/2}$	$3d_{5/2}$	$3d_{3/2}$	$2p_{3/2}$	$2p_{1/2}$
Mo-CZTS	931.2	951.0	486.0	494.5	1021.3	1044.4
Ti-CZTS	931.4	951.1	485.9	494.3	1021.3	1044.3

0.20 for Ti-CZTS and Mo-CZTS, respectively. Therefore, our obtained fit results are acceptable.

The presented S $2p$ spectrum of Fig. 13(d) consists of three doublets for Ti-CZTS. The S $2p_{3/2}$ peaks at 160.6 eV [58] and 161.0 eV [59] indicate monosulfide whereas the other at 162.2 eV represents disulfide (S_2^{2-}) [60].

Fig. 13(e) presents other positions of S $2p$ for Mo-CZTS. The existence of peaks at 161.1 eV [59] and 161.6 eV [60] interpret the monosulfide (S^{-2}) structure. The reason behind the higher binding energy of 161.6 eV than that observed in the literature is the increased coordination number of S atom [60]. The additional contribution obtained at 162.8 eV represents the formation of polysulfide (S_n^{2-}, where $2 \le n \le 8$) [61] which is generally observed in binding energy range between about 162.0 eV (disulfide) and 164.0 eV (elemental sulfur) [62].

When the EDS and XPS analyses were compared, a significant result related to the compositional contents was deduced. The composition derived from EDS measurements indicates that both films are Sn-rich but Zn-poor with sufficient sulfur inclusion. Moreover, XPS measurements pronounce a considerably Cu-poor and Sn-rich chemical surface structure with sufficient sulfur. Since EDS and XPS measurements are realized in different zones on the film surface, a small compositional variation was experienced. Even though XPS analysis for the CZTS surface layer does not give information associated with substrate interface, it gives valuable information about the existence of second phases and confirms the XRD, Raman and EDS analyses.

3.5. Optical properties

SLG-CZTS refers to a sample that was grown on an SLG substrate to measure the electrical and optical properties of the compound semiconductor thin film CZTS. The optical properties of the CZTS kesterite films were studied with transmission (T) and reflection (R) measurements at room temperature. The optical absorption coefficient (α) of the SLG-CZTS sample is obtained using the following formula [63]:

$$\alpha = \frac{1}{t} \ln \left[\frac{(1-R)^2}{T} \right] \tag{1}$$

where t is the thickness of the film. The optical band gap energy is obtained using the following equation [63]:

$$(\alpha h\nu) = A\left[h\nu - E_g\right]^n \tag{2}$$

where α is the optical absorption coefficient, A is a constant, E_g is the band gap energy, and n = 1/2 for direct allowed transition. The optical band gap energy was determined from the plot of $(\alpha h\nu)^2$ vs. photon energy ($h\nu$) by taking an intercept at the photon energy axis of the linear region extrapolation (Fig. 14). Straight line intercepting the photon energy axis gives the optical band gap energy, E_g, as 1.57 eV, which is in good agreement with the previously reported values [64]. The transmittance spectrum is given as an inset plot of Fig. 14.

3.6. Electrical properties

Van der Pauw and Hall effect methods were used to determine the electrical resistivity and the majority charge carriers, respectively. The
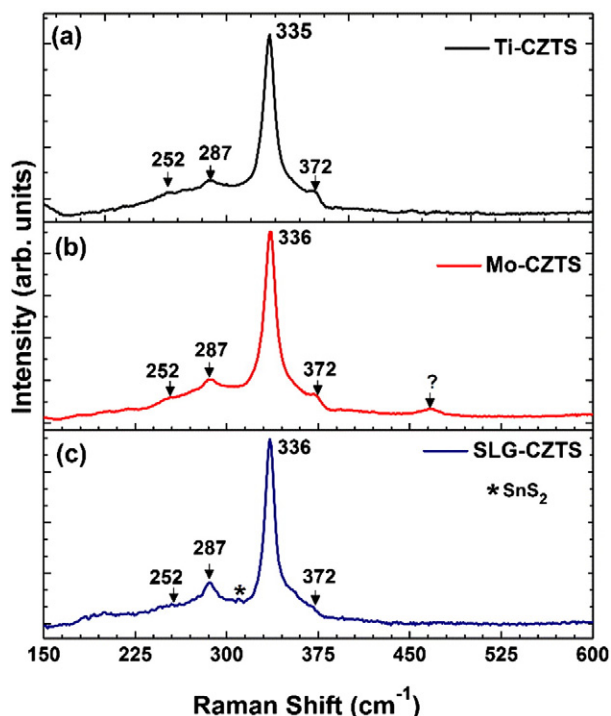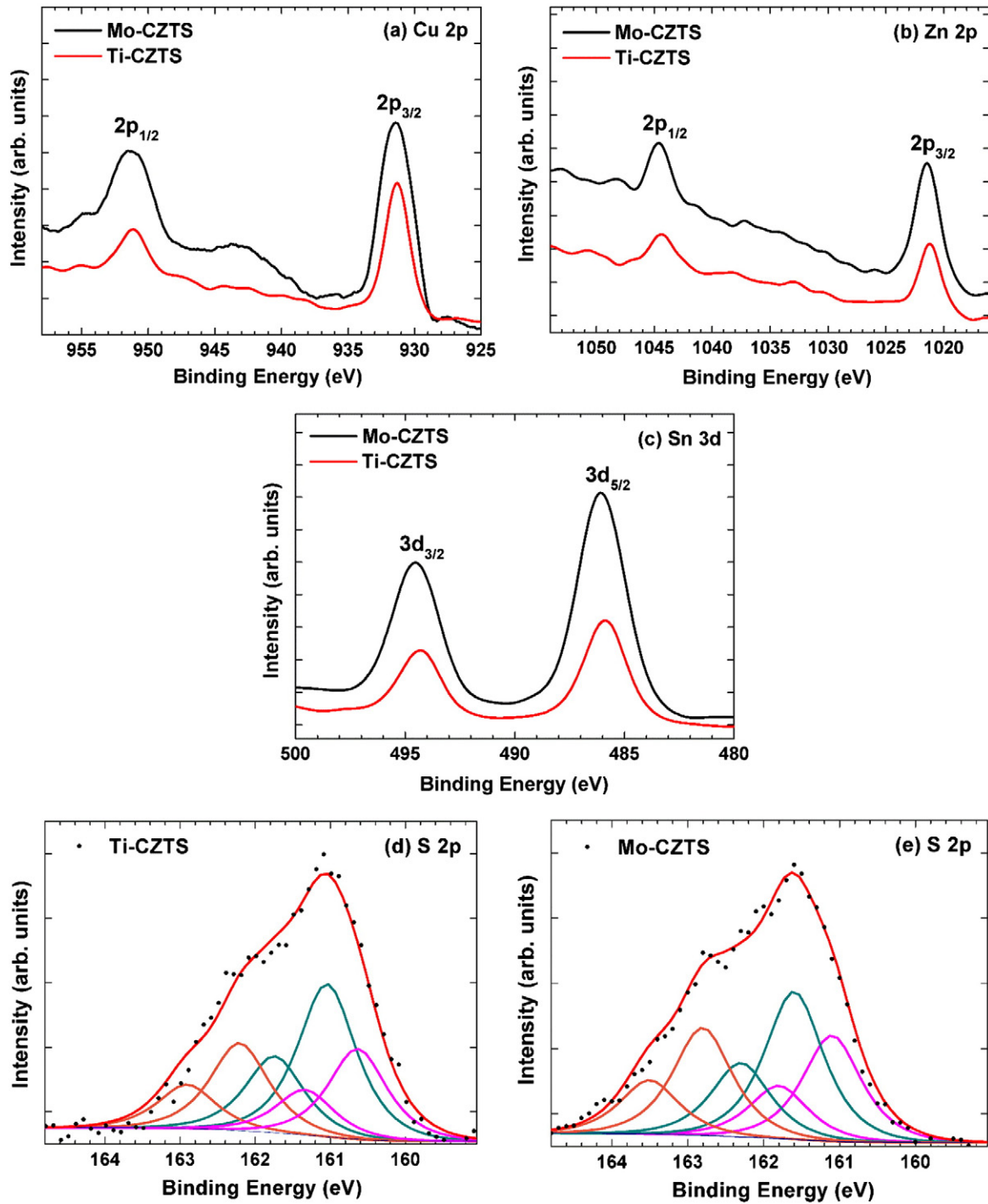
Fig. 13. XPS spectrum of CZTS thin films for the core-level spectra of (a) Cu 2p, (b) Zn 2p, (c) Sn 3d, (d) S 2p (Ti-CZTS) and (e) S 2p (Mo-CZTS).

Table 5
S 2p doublet parameters of the fit shown in Fig. 13(d) and (e) for sulfurized CZTS films of Ti-CZTS and Mo-CZTS, respectively.

		S $2p_{3/2}$ (eV)	Splitting (eV)	FWHM (eV)	Line shape
Mo-CZTS	Monosulfide	161.1	0.7	0.91	GL (80)
	Monosulfide	161.6	0.7	0.91	GL (80)
	Polysulfide	162.8	0.7	0.91	GL (80)
Ti-CZTS	Monosulfide	160.6	0.7	0.91	GL (80)
	Monosulfide	161.0	0.7	0.91	GL (80)
	Disulfide	162.2	0.7	0.91	GL (80)

SLG-CZTS sample was cut into small rectangular shapes using a diamond cutter. Film sheet resistance was measured between thin copper electrical contacts that were adhered to the film using silver epoxy. Sheet resistance and resistivity of the film at room temperature were measured as 244 $\Omega/\square$ and 0.024 $\Omega \cdot$cm, respectively. Patel et al. obtained similar results for CZTS prepared by a spray pyrolysis technique [65]. The type of conductivity was determined as p-type via Hall effect measurements. The carrier concentration was found as 6.8×10^{20} cm^{-3}, and the mobility of charge carriers was 0.40 cm^2/Vs. Even though the prevalent surface inhomogeneity problem of the CZTS layer makes the
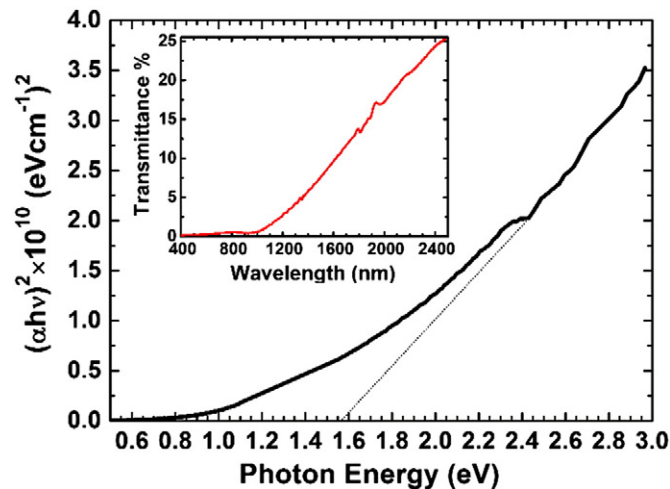
Fig. 14. The $(\alpha h\nu)^2$ vs. photon energy plot for optical band gap determination. The inset figure shows transmittance spectrum of CZTS on SLG.

interpretation of the electrical measurements rather complicated, the values of the carrier density were found to be in agreement with previous studies [66].

4. Conclusions

Since high-temperature sintering is required during the formation of an absorber layer, the choice of substrate is a very important issue. The substrate should be vacuum compatible and chemically inert to avoid any reactions with the chalcogens. The CTE of the substrate is also crucially important in the crack formation deduced by the SEM images of Mo-CZTS. Crack formation was detected on Mo-CZTS due to the mismatch between the thermal expansion coefficients of Mo and CZTS. Since uniform CZTS films without any degradations were grown on Ti foil with CTE in the range of $(8.4–8.6) \times 10^{-6}$ K^{-1}, it was concluded in this study that the Ti was the preferred foil with regard to its costs and physical properties.

Nearly pure CZTS layers were grown on Mo foil with the exception of Sn based secondary phases in XRD and the impurity peak at 460 cm^{-1} in the Raman spectra. In the Ti-CZTS sample, except local Sn-based crystal formation arising from Sn-rich composition, substrate material originated impurity peaks were not observed. This conclusion is consistent with XRD patterns of the samples. Because of small SLG-CZTS resistivity obtained from electrical characterization, the prepared samples can be used as an absorber layer in the fabrication of thin film solar cells.

Acknowledgments

References

[1] H. Katagiri, N. Sasaguchi, S. Hando, S. Hoshino, J. Ohashi, T. Yokota, Preparation and evaluation of Cu$_2$ZnSnS$_4$ thin films by sulfurization of E-B evaporated precursors, Sol. Energy Mater. Sol. Cells 49 (1997) 407–414.

[2] T. Kato, H. Hiroi, N. Sakai, S. Muraoka, H. Sugimoto, Proc. 27th Eur. Photovolt. Sol. Energy Conf 2012, pp. 2236–2239.

[3] W. Wang, M.T. Winkler, O. Gunawan, T. Gokmen, T.K. Todorov, Y. Zhu, D.B. Mitzi, Device characteristics of CZTSSe thin-film solar cells with 12.6% efficiency, Adv. Energy Mater. 4 (2013) 1301465.

[4] W. Shockley, H.J. Queisser, Detailed balance limit of efficiency of p–n junction solar cells, J. Appl. Phys. 32 (1961) 510–519.

[5] K. Ito, T. Nakazawa, Electrical and optical properties of stannite-type quaternary semiconductor thin films, Jpn. J. Appl. Phys. 27 (1988) 2094–2097.

[6] H. Araki, A. Mikaduki, Y. Kubo, T. Sato, K. Jimbo, W.S. Maw, H. Katagiri, M. Yamazaki, K. Oishi, A. Takeuchi, Preparation of Cu$_2$ZnSnS$_4$ thin films by sulfurization of stacked metallic layers, Thin Solid Films 517 (2008) 1457–1460.

[7] C. Shi, G. Shi, Z. Chen, P. Yang, M. Yao, Deposition of Cu$_2$ZnSnS$_4$ thin films by vacuum thermal evaporation from single quaternary compound source, Mater. Lett. 73 (2012) 89–91.

[8] K. Jimbo, R. Kimura, T. Kamimura, S. Yamada, W.S. Mav, H. Araki, K. Oishi, H. Katagiri, Cu$_2$ZnSnS$_4$-type thin film solar cells using abundant materials, Thin Solid Films 515 (2007) 5997–5999.

[9] T. Ericson, T. Kubbart, J.J. Scragg, C. Platzer-Björkman, Reactive sputtering of precursors for Cu$_2$ZnSnS$_4$ thin film solar cells, Thin Solid Films 520 (2012) 7093–7099.

[10] F. Liu, Y. Li, K. Zhang, B. Wang, C. Yan, Y. Lai, Z. Zhang, J. Lie, Y. Lu, In situ growth of Cu$_2$ZnSnS$_4$ thin films by reactive magnetron co-sputtering, Sol. Energy Mater. Sol. Cells 94 (2010) 2431–2434.

[11] P.A. Fernandes, P.M.P. Salome, A.F. De Cunha, Growth and Raman scattering characterization of Cu$_2$ZnSnS$_4$ thin films, Thin Solid Films 517 (2009) 2519–2523.

[12] J.J. Scragg, P.J. Dale, L.M. Peter, Towards sustainable materials for solar energy conversion: preparation and photoelectrochemical characterization of Cu$_2$ZnSnS$_4$, Electrochem. Commun. 10 (2008) 639–642.

[13] A. Ennaoui, M. Lux-Steiner, A. Weber, D. Abou-Ras, I. Kötschau, H.-W. Schock, R. Schurr, A. Hölzing, S. Jost, R. Hock, T. Voβ, J. Schulze, A. Kirbs, Cu$_2$ZnSnS$_4$ thin film solar cells from electroplated precursors: novel low-cost perspective, Thin Solid Films 517 (2009) 2511–2514.

[14] K. Tanaka, M. Kato, K. Goto, Y. Nakano, H. Uchik, Face-to-face annealing process of Cu2ZnSnS4 thin films deposited by spray pyrolysis method, Jpn. J. Appl. Phys. 51 (2012) (10NC26-1-10NC26-4).

[15] H. Yoo, J. Kim, Comparative study of Cu$_2$ZnSnS$_4$ film growth, Sol. Energy Mater. Sol. Cells 95 (2011) 239–244.

[16] A.V. Moholkar, S.S. Shinde, A.R. Babar, K. Sim, Y. Kwon, K.Y. Rajpure, P.S. Patil, C.H. Bhosale, J.H. Kimb, Development of CZTS thin films solar cells by pulsed laser deposition: influence of pulse repetition rate, Sol. Energy 85 (2011) 1354–1363.

[17] M. Winkler, J. Griesche, I. Konovalov, J. Penndorf, J. Wienke, O. Tober, CISCuT—solar cells and modules on the basis of CuInS$_2$ on Cu-tape, Sol. Energy 77 (2004) 705–716.

[18] F. Kessler, D. Rudmann, Technological aspects of flexible CIGS solar cells and modules, Sol. Energy 77 (2004) 685–695.

[19] P. Dai, G. Zhang, Y. Chen, H. Jiang, Z. Feng, Z. Lin, J. Zhan, Porous copper zinc tin sulfide thin film as photocathode for double junction photoelectrochemical solar cells, Chem. Commun. 48 (2012) 3006–3008.

[20] Z. Zhou, Y. Wang, D. Xu, Y. Zhang, Fabrication of Cu$_2$ZnSnS$_4$ screen printed layers for solar cells, Sol. Energy Mater. Sol. Cells 94 (2010) 2042–2045.

[21] M. Farinella, R. Inguantaa, T. Spanòa, P. Livrerib, S. Piazzaa, C. Sunseria, Electrochemical deposition of CZTS thin films on flexible substrate, Energy Procedia 44 (2014) 105–110.

[22] J.J. Scragg, J.T. Watjen, M. Efoff, T. Ericson, T. Kubart, C. Platzer-Björkman, A detrimental reaction at the molybdenum back contact in Cu2ZnSn(S, Se)4 thin-film solar cells, J. Am. Chem. Soc. 134 (2012) 19330–19333.

[23] J.J. Scragg, T. Kubart, J.T. Watjen, T. Ericson, M.K. Linnarsson, C. Platzer-Björkman, Effects of back contact instability on Cu$_2$ZnSnS$_4$ devices and process, Chem. Mater. 25 (2013) 3162–3171.

[24] K.J. Yang, J.H. Sim, B. Jeon, D.H. Son, D.H. Kim, S.J. Sung, D.K. Hwang, S. Song, D.B. Khadka, J. Kim, J.K. Kang, Effects of Na and MoS$_2$ on Cu$_2$ZnSnS$_4$ thin-film solar cell, Prog. Photovolt. Res. Appl. (2014) http://dx.doi.org/10.1002/pip.2500.

[25] M. Hartmann, M. Schmidt, A. Jasenek, H.W. Schock, F. Kessler, K. Herz, M. Powalla, Flexible and lightweight substrates for Cu(In,Ga)Se$_2$ solar cells and modules, Proceeding of the 28th IEEE Photovoltaic Specialists Conference, Anchorage, Alaska 2000, pp. 638–641.

[26] T. Yagioka, T. Nakada, Cd-free flexible Cu(In, Ga)Se2 thin film solar cells with ZnS(O, OH) buffer layers on Ti foils, Appl. Phys. Express 2 (2009) 072201–072203.

[27] A. Zhecheva, W. Sha, S. Malinov, A. Long, Enhancing the microstructure and properties of titanium alloys through nitriding and other surface engineering methods, Surf. Coat. Technol. 200 (2005) 2192–2207.

[28] M. Jiang, X. Yan, Cu$_2$ZnSnS$_4$ thin film solar cells: present status and future prospects, in: A. Morales-Acevedo (Ed.), Solar Cells — Research and Application Perspectives, InTech, Croatia 2013, pp. 107–145.

[29] A.V. Briones, T. Sato, U.G. Bigol, Antibacterial activity of polyethylenimine/carrageenan multilayer against pathogenic bacteria, Adv. Chem. Eng. Sci. 4 (2014) 233–241.

[30] J. Pouilleau, D. Devilliers, F. Garrido, S. Durand-Vidal, E. Mahe, Structure and composition of passive titanium oxide films, Mater. Sci. Eng. B 47 (1997) 235–243.

[31] E. Gemelli, N.H.A. Camargo, Oxidation kinetics of commercially pure titanium, Rev. Mater. 12 (2007) 525–531.

[32] Perrin Walker, William H. Tarn, Handbook of Metal Etchants, CRC Press, 1991.

[33] M. Takeuchi, Y. Abe, Y. Yoshida, Y. Nakayama, M. Okazakid, Y. Akagawa, Acid pretreatment of titanium implants, Biomaterials 24 (2003) 1821–1827.

[34] D. Krishnamurti, The raman spectrum of rutile, Proc. Indian Acad. Sci. Sect. A 55 (1962) 290–299.

[35] D.B. Mitzi, O. Gunawan, T.K. Todorov, K. Wang, S. Guha, The path towards a high-performance solution-processed kesterite solar cell, Sol. Energy Mater. Sol. Cells 95 (2011) 1421–1436.

[36] H. Katagiri, N. Ishigaki, T. Ishida, K. Saito, Characterization of Cu$_2$ZnSnS$_4$ thin films prepared by vapor phase sulfurization, Jpn. J. Appl. Phys. 40 (2001) 500–504.

[37] C. Platzer-Björkman, J. Scragg, H. Flammersberger, T. Kubart, M. Edoff, Influence of precursor sulfur content on film formation and compositional changes in Cu$_2$ZnSnS$_4$ films and solar cells, Sol. Energy Mater. Sol. Cells 98 (2012) 110–117.

[38] H. Katagiri, K. Saitoh, T. Washio, H. Shinohara, T. Kurumadani, S. Miyajima, Development of thin film solar cell based on Cu_2ZnSnS_4 thin films, Sol. Energy Mater. Sol. Cells 65 (1) (2001) 141–148.

[39] B.D.J. Louis, Investigation and Development of CIGS Solar Cells on Flexible Substrates and With Alternative Electrical Back Contacts Presented by, ETH Zurich(Doctor of Sciences Thesis) 2009.

[40] A.J. Cheng, M. Manno, A. Khare, C. Leighton, S.A. Campbell, E.S. Aydil, Imaging and phase identification of Cu_2ZnSnS_4 thin films using confocal Raman spectroscopy, J. Vac. Sci. Technol. A 29 (5) (2011) 051203–051211.

[41] X. Fontané, L. Calvo-Barrio, V. Izquierdo-Roca, E. Saucedo, A. Pérez-Rodriguez, J.R. Morante, D.M. Berg, P.J. Dale, S. Siebentritt, In-depth resolved Raman scattering analysis for the identification of secondary phases: characterization of Cu_2ZnSnS_4 layers for solar cell applications, Appl. Phys. Lett. 98 (2011) 181905–181907.

[42] M. Ganchev, J. Iljina, L. Kaupmees, T. Raadik, O. Volobujeva, A. Mere, M. Altosaar, J. Raudoja, E. Mellikov, Phase composition of selenized $Cu_2ZnSnSe_4$ thin films determined by X-ray diffraction and Raman spectroscopy, Thin Solid Films 519 (2011) 7394–7398.

[43] L.S. Price, I.P. Parkin, A.M.E. Hardy, R.J.H. Clark, Atmospheric pressure chemical vapour deposition of tin sulfides (SnS, Sn_2S_3, SnS_2) on glass, Chem. Mater. 11 (1999) 1792–1799.

[44] P.A. Fernandes, P.M.P. Salomé, F.D. Cunha, A study of ternary Cu_2SnS_3 and Cu_3SnS_4 thin films prepared by sulfurizing stacked metal precursors, J. Phys. D 43 (2010) 215403–215413.

[45] M. Altosaar, J. Raudoja, K. Timmo, M. Danilson, M. Grossberg, J. Krustok, E. Mellikov, $Cu_2Zn_{1-x}Cd_xSn(Se_{1-y}S_y)_4$ solid solutions as absorber materials for solar cells, Phys. Status Solidi A 205 (2008) 167–170.

[46] S. Sarkar, K. Bhattacharjee, G.C. Das, K.K. Chattopadhyay, Self-sacrificial template directed hydrothermal route to kesterite-Cu_2ZnSnS_4 microspheres and study of their photo response properties, CrystEngComm 16 (2014) 2634–2644.

[47] F. Jiang, H. Shen, W. Wang, Optical and electrical properties of Cu_2ZnSnS_4 film prepared by sulfurization method, J. Electron. Mater. 41 (2012) 2204–2209.

[48] X. Yin, C. Tang, M. Chen, S. Adams, H. Wang, H. Gong, Hierarchical porous Cu_2ZnSnS_4 films for high-capacity reversible lithium storage applications, J. Mater. Chem. A 1 (2013) 7927–7932.

[49] S.S. Mali, B.M. Patil, C.A. Betty, P.N. Bhosale, Y.W. Oh, S.R. Jadkar, R.S. Devan, Y.-R. Ma, P.S. Patil, Novel synthesis of kesterite Cu_2ZnSnS_4 nanoflakes by successive ionic layer adsorption and reaction technique: characterization and application, Electrochim. Acta 66 (2012) 216–221.

[50] C.L.A. Ricardo, M.S. Su'ait, M. Müller, P. Scardi, Production of Cu2(Zn, Fe)SnS4 powders for thin film solar cell by high energy ball milling, J. Power Sources 230 (2013) 70–75.

[51] M. Edler, T. Rath, A. Schenk, A. Fischereder, W. Haas, B. Chernev, B. Kunert, F. Hofer, R. Resel, G. Trimmel, Copper zinc tin sulfide layers prepared from solution processable metal dithiocarbamate precursors, Mater. Chem. Phys. 136 (2012) 582–588.

[52] C.D. Wagner, W.M. Riggs, L.E. Davis, J.F. Moulder, in: G.E. Muilenberg (Ed.), Handbook of X-Ray Photoelectron Spectroscopy, Perkin-Elmer Corporation (Physical Electronics), Minnesota 1979, pp. 84–85.

[53] S. Das, C. Frye, P.G. Muzykov, K.C. Mandal, Deposition and characterization of low-cost spray pyrolyzed Cu_2ZnSnS_4 (CZTS) thin-films for large-area high-efficiency heterojunction solar cells, ECS Trans. 45 (2012) 153–161.

[54] B.S. Pawar, S.M. Pawar, S.W. Shin, D.S. Choi, C.J. Park, S.S. Kolekar, J.H. Kim, Effect of complexing agent on the properties of electrochemically deposited Cu_2ZnSnS_4 thin films, Appl. Surf. Sci. 257 (2010) 1786–1791.

[55] S. Das, K.C. Mandal, Comparison of Cu_2ZnSnS_4 Thin Film Properties Prepared by Thermal Evaporation of Elemental Metals and Binary Sulfide Sources, IEEE, 2011. 2674–2678.

[56] M. Cruz, J. Morales, J.P. Espinos, J. Sanzc, XRD, XPS and ^{119}Sn NMR study of tin sulfides obtained by using chemical vapor transport methods, J. Solid State Chem. 175 (2003) 359–365.

[57] A.M. Tripathi, S. Mitra, Tin sulfide (SnS) nanorods: structural, optical and lithium storage property study, RSC Adv. 4 (2014) 10358–10366.

[58] S.L. Harmer, J.E. Thomas, D. Fornasiero, A.R. Gerson, The evolution of surface layers formed during chalcopyrite leaching, Geochim. Cosmochim. Acta 70 (2006) 4392–4402.

[59] A. Ghahremaninezhad, D.G. Dixon, E. Asselin, Electrochemical and XPS analysis of chalcopyrite ($CuFeS_2$) dissolution in sulfuric acid solution, Electrochim. Acta 87 (2013) 97–112.

[60] R.G. Acres, S.L. Harmer, D.A. Beattie, Synchrotron XPS studies of solution exposed chalcopyrite, bornite, and heteregeneous chalcopyrite with bornite, Int. J. Miner. Process. 94 (2010) 43–51.

[61] X. Liang, C. Hart, Q. Pang, A. Garsuch, T. Weiss, L.F. Nazar, A highly efficient polysulfide mediator for lithium–sulfur batteries, Nat. Commun. 6 (2015) 5682–5690.

[62] D.L. Legrand, H.W. Nesbitt, G.M. Bancroft, X-ray photoelectron spectroscopic study of a pristine millerite (NiS) surface and the effect of air and water oxidation, Am. Mineral. 83 (1998) 1256–1265.

[63] J.I. Pankove, Optical Processes in Semiconductors, Dover Inc., New York, 1975.

[64] X. Li, D. Wang, Q. Du, W. Liu, G. Jiang, C. Zhu, Growth of Cu_2ZnSnS_4 thin films by sulfurization of co-sputtered metallic precursors, Adv. Mater. Res. 418–420 (2012) 67–71.

[65] M. Patel, I. Mukhopadhyay, A. Ray, Structural, optical and electrical properties of spray-deposited CZTS thin films under a non-equilibrium growth condition, J. Phys. D. Appl. Phys. 45 (2012) 445103 (1–10).

[66] V.G. Rajeshmon, C.S. Kartha, K.P. Vijayakumar, C. Sanjeeviraja, T. Abe, Y. Kashiwaba, Role of precursor in solution in controlling the opto-electronic properties of spray-pyrolsed Cu_2ZnSnS_4 thin films, Sol. Energy 85 (2011) 249–255.